Quan Zhang, Qun Wei*, Haiyan Yan, Qingyang Fan, Xuanmin Zhu, Junqin Zhang and Dongyun Zhang

Mechanical and Electronic Properties of $P4_2/mnm$ Silicon Carbides

DOI 10.1515/zna-2015-0539
Received December 26, 2015; accepted January 20, 2016

Abstract: Two new phases of Si_8C_4 and Si_4C_8 with the $P4_2/mnm$ symmetry are proposed. Using first principles calculations based on density functional theory, the structural, elastic, and electronic properties of Si_8C_4 and Si_4C_8 are studied systematically. Both Si_8C_4 and Si_4C_8 are proved to be mechanically and dynamically stable. The elastic anisotropies of Si_8C_4 and Si_4C_8 are studied in detail. Electronic structure calculations show that Si_8C_4 and Si_4C_8 are indirect semiconductors with the band gap of 0.74 and 0.15 eV, respectively.

Keywords: Elastic Properties; Electronic Properties; First Principles Calculations; Silicon Carbides.

1 Introduction

It is known that semiconductor materials have attracted a large amount of interest, and they have been applied widely in information technology areas. As a third-generation semiconductor material, SiC has been widely studied [1–10]. As known, the group 14 elements have many structural phases at different conditions [11–13], so there are a large number of polytypes for the SiC crystal [2]. The polytypes can be divided into three groups, namely, cubic (C), hexagonal (H), and rhombohedral (R) structures. And, the 3C polytype (β-SiC) with a zincblende structure is the most simple polytype.

Recently, the nanoparticle SiC was used in superconductor to enhance the critical current density [7]. It is proved that the addition of nanosized SiC particles in the ultra-high-temperature ceramics can not only impart a better oxidation resistance but also improve the flexural strength [8]. Lomello et al. studied the processing of nano-SiC ceramics to establish a correlation between the microstructural features and the mechanical behaviour [9]. Furthermore, Wang et al. reported a new temperature-dependent fracture strength model for the ZrB_2–SiC composites [10]. In recent years, the graphene extremely appeals for a wide range of applications [14, 15]. To make the large-area epitaxial grapheme samples and the large-scale production of graphene-based devices appear feasible, many works about the epitaxial graphene on SiC have been performed [16–19], and they all obtained the considerable achievements. With the development of technology, more and more new structures of silicon carbides are constantly presented. By using genetic algorithm, the novel low-energy sp^3-hybridised framework structure of the group 14 elements was proposed, which is a cagelike distorted tetragonal structure consisting of 12 atoms per unit cell with the $P4_2/mnm$ (No. 136) symmetry [20].

For $P4_2/mnm$-Si, the Si atoms occupy 4*d* and 8*j* Wyckoff positions. We replace the Si atoms by C atoms at 4*d* and 8*j* positions, respectively, and then two structures of Si_8C_4 and Si_4C_8 are obtained. In the present article, we studied the structural, elastic, and electronic properties of Si_8C_4 and Si_4C_8 systematically.

2 Computational Method

Based on the first principles calculations, the structural optimisations of the $P4_2/mnm$ silicon carbides were performed using the density functional theory (DFT) [21, 22] with the local density approximation (LDA) [23, 24], and the generalised gradient approximation (GGA) parameterised by Perdew, Burke, and Ernzerrof (PBE) [25] as implemented in the Cambridge Serial Total Energy Package (CASTEP) code [26]. The Broyden–Fletcher–Goldfarb–Shanno (BFGS) [27] minimisation scheme was used in

***Corresponding author: Qun Wei,** School of Physics and Optoelectronic Engineering, Xidian University, Xi'an 710071, PR China, E-mail: weiaqun@163.com
Quan Zhang, Qingyang Fan and Junqin Zhang: School of Microelectronics, Xidian University, Xi'an 710071, PR China
Haiyan Yan: School of Chemistry and Chemical Engineering, Baoji University of Arts and Sciences, Baoji 721013, PR. China
Xuanmin Zhu: School of Physics and Optoelectronic Engineering, Xidian University, Xi'an 710071, PR China
Dongyun Zhang: National Supercomputing Center in Shenzhen, Shenzhen 518055, PR China

geometry optimisation. When the total energy is 5.0×10^{-6} eV/atom, the maximum ionic Hellmann–Feynman force is 0.01 eV/Å, the maximum stress is 0.02 GPa, and the maximum ionic displacement is 5.0×10^{-4} Å, the structural relaxation will stop. For Si_{12}, Si_8C_4, Si_4C_8, and C_{12}, the energy cutoff is 390, 390, 390, and 410 eV, respectively. For the Brillouin-zone sampling, the Monkhorst–Pack scheme [28] is $5\times5\times3$, $6\times6\times3$, $6\times6\times4$, and $5\times5\times3$ for Si_{12}, Si_8C_4, Si_4C_8, and C_{12}, respectively.

3 Results and Discussions

3.1 Structural Properties

The crystal structure with 12 atoms per unit cell, the X_{24} rugby ball unit and the $1\times2\times2$ supercell structure of $P4_2/mnm$ silicon carbides are illustrated in Figure 1. The black and blue spheres represent C and Si atoms, respectively. Figure 1(a), (b), and (c) are for Si_8C_4, and Figure 1(d), (e), and (f) are for Si_4C_8. The $P4_2/mnm$ structure is a cage-like distorted sp^3-hybridised framework structure. The X_{24} rugby ball unit (shown in Fig. 1(b) and (e)) has two square, eight pentagonal, and four hexagonal faces. It can form a crystal by the X_{24} rugby balls with sharing faces. As seen in Figure 1(c), one can find that, for Si_8C_4, the Si atom bonded with two C atoms and two Si atoms, the C atom bonded with four adjacent Si atoms. By contrast, for Si_4C_8 in Figure 1(f), the Si atom bonded with four adjacent C atoms and the C atom bonded with two C atoms and two Si atoms. Furthermore, along *c*-axis, the rugby ball unit connects with each other by the Si–Si or C–C bonds, respectively. Along the *a*- and *b*-axes, the rugby ball unit connects with each other by sharing the hexagonal face.

The calculated atomic positions of $P4_2/mnm$ structures are listed in Table 1. The lattice parameters and the specific bond lengths of $P4_2/mnm$ structures are presented

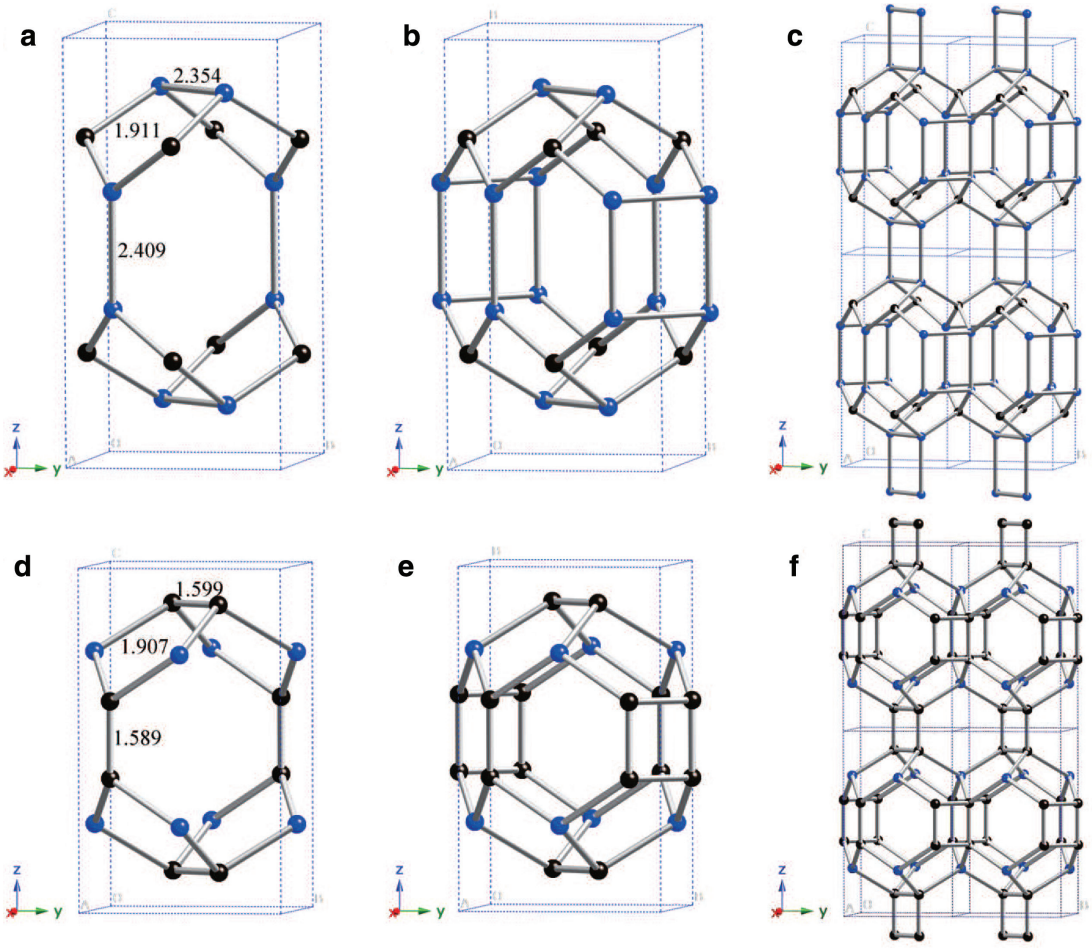

Figure 1: (Color online) (a) Crystal structure with 12 atoms per unit cell for Si_8C_4. (b) The X_{24} rugby ball unit for Si_8C_4. (c) The $1\times2\times2$ supercell structure for Si_8C_4. (d), (e), and (f) are for Si_4C_8. The black and blue spheres represent C and Si atoms, respectively.

Table 1: The atomic positions of $P4_2/mnm$ structures.

Atom		Wyckoff positions	
		4*d*	8*j*
Si_{12}	Si	(0.00000, 0.50000, 0.25000)	(0.34405, 0.34405, 0.12360)
Si_8C_4	C	(0.00000, 0.50000, 0.25000)	
	Si		(0.31372, 0.31372, 0.13672)
Si_4C_8	C		(0.36551, 0.36551, 0.11204)
	Si	(0.00000, 0.50000, 0.25000)	
C_{12}	C	(0.00000, 0.50000, 0.25000)	(0.34588, 0.34588, 0.12450)

in Table 2. Compared with the previous results of Si_{12} and C_{12} [20], our calculations are in an excellent agreement with them. We can find that there are three kinds of bond lengths for each structure; the Si_{12} and C_{12} have three kinds of Si–Si bonds and C–C bonds, respectively; the Si_8C_4 has two kinds of Si–Si bonds and one kind of Si–C bond; and the Si_4C_8 has two kinds of C–C bonds and one kind of Si–C bond. Furthermore, the lattice parameters *a* and *c*, the cell volume per formula unit V_0, and the bond lengths are decreasing with the decrease of Si atoms.

3.2 Elastic Properties and Anisotropy

It is known that the elastic constants are important to the mechanical properties in practical applications. Because the bond energy of C–C bond is larger than that of Si–Si bond, we can expect that the elastic constants of Si_4C_8 are larger than those of Si_8C_4. The calculated crystal elastic constants C_{ij} are shown in Table 3. Obviously, it conforms our expectation, the more the C–C bonds, the larger the elastic constants. And, C_{33} is larger than C_{11}, indicating along the *c*-axis direction, the Si_8C_4 and Si_4C_8 have better incompressibility. In addition, for a stable tetragonal structure, the criteria for mechanical stability are given by [29]

$$C_{ii}>0,\ i=1,\ 3,\ 4,\ 6, \tag{1}$$

$$(C_{11}-C_{22})>0, \tag{2}$$

$$(C_{11}+C_{33}-2C_{13})>0, \tag{3}$$

$$[2(C_{11}+C_{12})+C_{33}+4C_{13}]>0. \tag{4}$$

The calculated elastic constants of Si_{12}, Si_8C_4, Si_4C_8, and C_{12} are all satisfied to above formulas, indicating that these structures are mechanically stable. Previous phonon calculations for Si_{12} and C_{12} have confirmed that they are dynamically stable [20]. To ensure the dynamical stability of $P4_2/mnm$ silicon carbides, we calculated the phonon spectra of Si_8C_4 and Si_4C_8 (see Fig. 2). As seen, there is no imaginary frequency in the whole Brillouin zone, so we could conclude that Si_8C_4 and Si_4C_8 are dynamically stable.

The average bulk modulus *B*, shear modulus *G*, Young's modulus *E*, and Poisson's ratio *ν* calculated by the Voigt–Reuss–Hill approximations [30–32] and the *B*/*G* ratio are shown in Table 3. The Voigt bound is obtained by the average polycrystalline modulus based on an assumption of uniform strain throughout a polycrystalline and is the upper limit of the actual effective modulus. We can obtain the B_V and G_V from the elastic constants C_{ij} [30]:

$$B_V=\frac{1}{9}[C_{11}+C_{22}+C_{33}+2(C_{12}+C_{13}+C_{23})], \tag{5}$$

$$G_V=\frac{1}{15}[C_{11}+C_{22}+C_{33}+3(C_{44}+C_{55}+C_{66})-(C_{12}+C_{13}+C_{23})]. \tag{6}$$

The Reuss bound is obtained by assuming a uniform stress and is the lower limit of the actual effective

Table 2: The lattice parameters *a*, *c* (in Å), cell volume per formula unit V_0 (in Å^3), and bond lengths (in Å).

	a	*c*	V_0	Bond lengths						
						Si–Si	Si–C			C–C
Si_{12}	5.380	9.661	279.620	2.371	2.373	2.388				
	5.388[a]	9.629[a]		2.371[a]	2.374[a]	2.384[a]				
Si_8C_4	4.468	8.810	175.882	2.354	2.409		1.911			
Si_4C_8	4.203	7.092	125.258				1.907	1.599	1.589	
C_{12}	3.526	6.276	78.407					1.550	1.537	1.563
	3.530[a]	6.290[a]								

[a][20].

Table 3: Calculated elastic constants C_{ij} (GPa), bulk modulus B (GPa), shear modulus G (GPa), Young's modulus E (GPa), Poisson's ratio ν, and B/G ratio.

	C_{11}	C_{33}	C_{44}	C_{66}	C_{12}	C_{13}	B	G	E	ν	B/G
Si_{12}	114	137	43	52	38	53	72	42	106	0.256	1.72
Si_8C_4	200	253	72	115	65	87	124	78	194	0.240	1.59
Si_4C_8	386	452	180	183	91	109	204	169	397	0.175	1.21
C_{12}	806	851	375	459	71	145	353	379	837	0.105	0.93

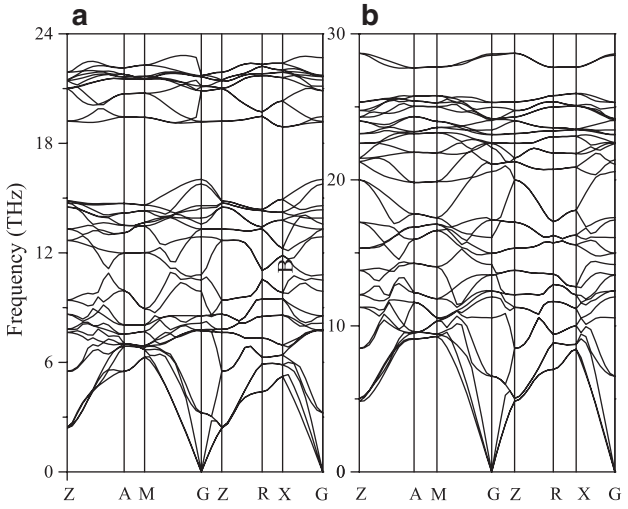

Figure 2: The phonon spectra of Si_8C_4 (a) and Si_4C_8 (b).

modulus. We can obtain the B_R and G_R from the elastic constants C_{ij} [31]:

$$B_R=\Delta[C_{11}(C_{22}+C_{33}-2C_{23})+C_{22}(C_{33}-2C_{13})-2C_{33}C_{12}+C_{12}(2C_{23}-C_{12})+C_{13}(2C_{12}-C_{13})+C_{23}(2C_{13}-C_{23})]^{-1}, \quad (7)$$

$$G_R=15\{4[C_{11}(C_{22}+C_{33}+C_{23})+C_{22}(C_{33}+C_{13})+C_{33}C_{12}-C_{12}(C_{23}+C_{12})-C_{13}(C_{12}+C_{13})-C_{23}(C_{13}+C_{23})]/\Delta+3\left(\frac{1}{C_{44}}+\frac{1}{C_{55}}+\frac{1}{C_{66}}\right)\}^{-1}, \quad (8)$$

where

$$\Delta=C_{13}(C_{12}C_{23}-C_{13}C_{22})+C_{23}(C_{12}C_{13}-C_{23}C_{11})+C_{33}(C_{11}C_{22}-C_{12}^2). \quad (9)$$

The arithmetic average of them is called Voigt–Reuss–Hill approximations, and we can obtain the B and G [32]:

$$B=\frac{1}{2}(B_V+B_R),\ G=\frac{1}{2}(G_V+G_R). \quad (10)$$

where subscript V denotes the Voigt bound, and R denotes the Reuss bound.

Typically, after the deformation, we can extrapolate the hardness from the size of indentation. For a hard material, the high bulk modulus can support the decrease of volume, and the high shear modulus can ensure that the deformation of the material will be in a right direction created by the applied load. So, the bulk and shear modulus are pretty important while analysing the properties of materials. The calculated bulk modulus of Si_8C_4 is 124 GPa, which is larger than that of Si_{12} (72 GPa) and smaller than that of Si_4C_8 (204 GPa) and C_{12} (353 GPa). This suggests that the Si_4C_8 has a stronger ability to resist the uniform compression than Si_8C_4, and the ability of C_{12} is the strongest. According to Teter [33], the shear modulus is a better parameter to qualitatively predict the hardness to a large extent. So, from Table 3, we can find that the shear modulus of Si_{12} (42 GPa) is the smallest, and it is about 46 %, 75 %, and 89 % smaller than that of Si_8C_4 (78 GPa), Si_4C_8 (169 GPa) and C_{12} (379 GPa), respectively, indicating that with the diminishing content of Si atoms, the hardness is increased.

For crystal physics and engineering science, the fracture resistance is represented by the bulk modulus B, and the plastic deformation resistance is represented by the shear modulus G. The ratio of bulk to shear modulus (B/G) proposed by Pugh [34] is an indication of ductile or brittle character. The high B/G ratio is associated with ductility, whereas the low value corresponds to brittle nature. If $B/G>1.75$, the material behaves in a ductile way [35]; otherwise, the material behaves in a brittle way. From Table 3, it can be seen that the B/G ratio of $P4_2/mnm$ phase Si_{12}, Si_8C_4, Si_4C_8, and C_{12} is 1.72, 1.59, 1.21, and 0.93, respectively, which is all <1.75. Thereby, the $P4_2/mnm$ phase Si_{12}, Si_8C_4, Si_4C_8, and C_{12} all are brittle.

To get more information about the elastic properties, Young's modulus E and Poisson's ratio ν are calculated. As a measure of the stiffness of a solid material, Young's modulus E is defined as the ratio between stress and strain. And, when a material receives the tension or compression in unidirectional, the absolute value of the ratio of transverse contraction strain to longitudinal extension strain is called Poisson's ratio ν. They are given by the following equations [32]:

$$E=\frac{9BG}{3B+G},\quad \nu=\frac{3B-2G}{2(3B+G)}. \quad (11)$$

From Table 3, we can find that Young's modulus of Si_8C_4 (194 GPa) is 83 % larger than that of Si_{12} (106 GPa), and 51 % and 77 % smaller than that of Si_4C_8 (397 GPa) and C_{12} (837 GPa), respectively. Si_4C_8 has a higher stiffness, compared with Si_8C_4. Poisson's ratio of Si_8C_4 (0.24) is 6 % smaller than that of Si_{12} (0.256), and 37 % and 129 % larger than that of Si_4C_8 (0.175) and C_{12} (0.105), respectively.

The anisotropy of the bulk modulus along the *a*- and *c*-axes with respect to *b*-axis can be estimated by

$$A_{B_a} = \frac{B_a}{B_b}, \quad A_{B_c} = \frac{B_c}{B_b}. \tag{12}$$

If the values are not 1.0, representing the elastic anisotropy. B_a, B_b, and B_c are the bulk modulus along the *a*-, *b*- and *c*-axes, respectively, which can be calculated as follows [36]:

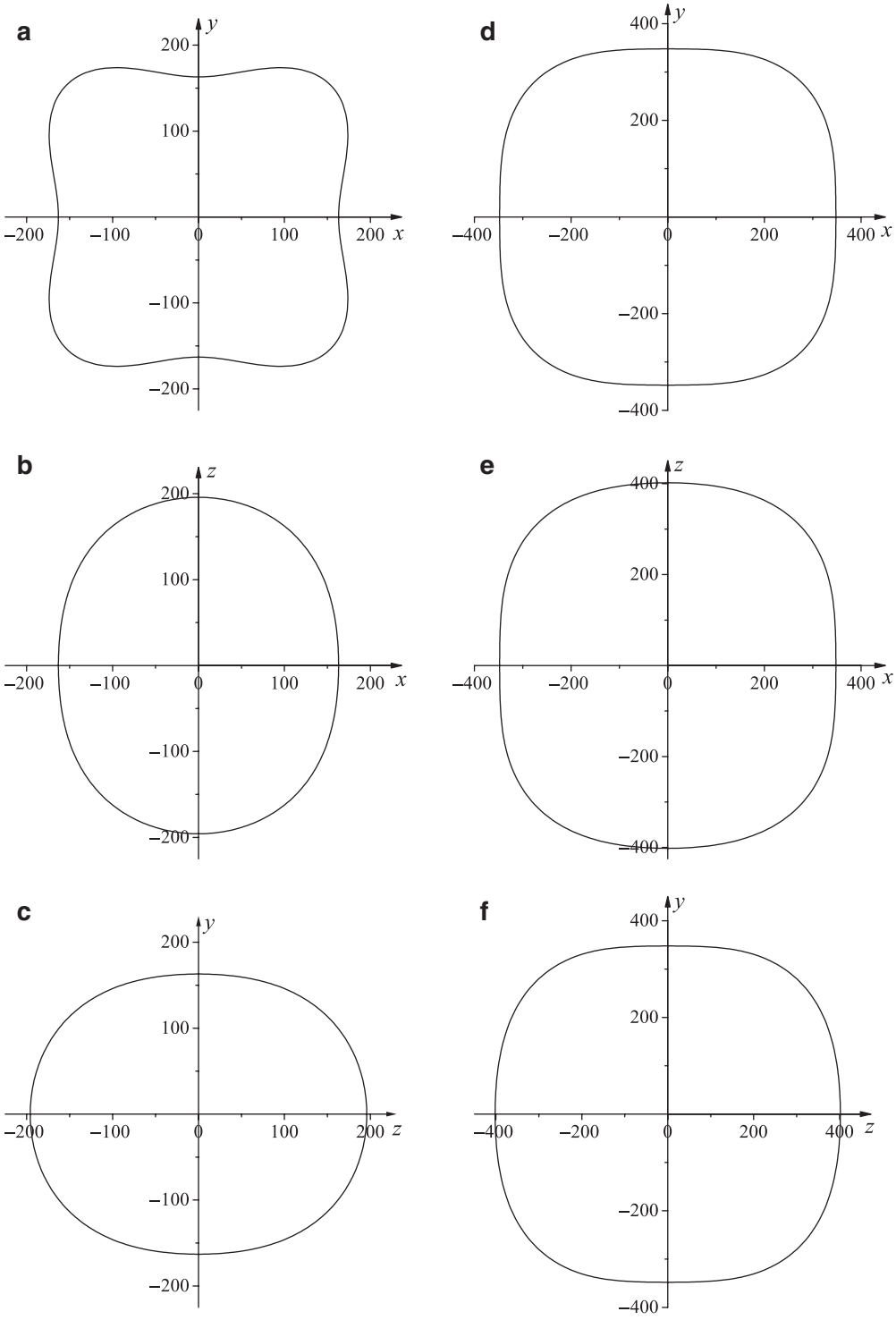

Figure 3: Two-dimensional representation of Young's modulus in the *xy* plane, *xz* plane, and *yz* plane for $P4_2/mnm$ silicon carbides. The left column (a), (b), and (c) are for Si_8C_4, and the right column (d), (e), and (f) are for Si_4C_8.

$$B_a = a\frac{dP}{da} = \frac{\Lambda}{1+\alpha+\beta}, \quad (13)$$

$$B_b = b\frac{dP}{db} = \frac{B_a}{\alpha}, \quad (14)$$

$$B_c = c\frac{dP}{dc} = \frac{B_a}{\beta}, \quad (15)$$

where

$$\Lambda = C_{11} + 2C_{12}\alpha + C_{22}\alpha^2 + 2C_{13}\beta + C_{33}\beta^2 + 2C_{23}\alpha\beta, \quad (16)$$

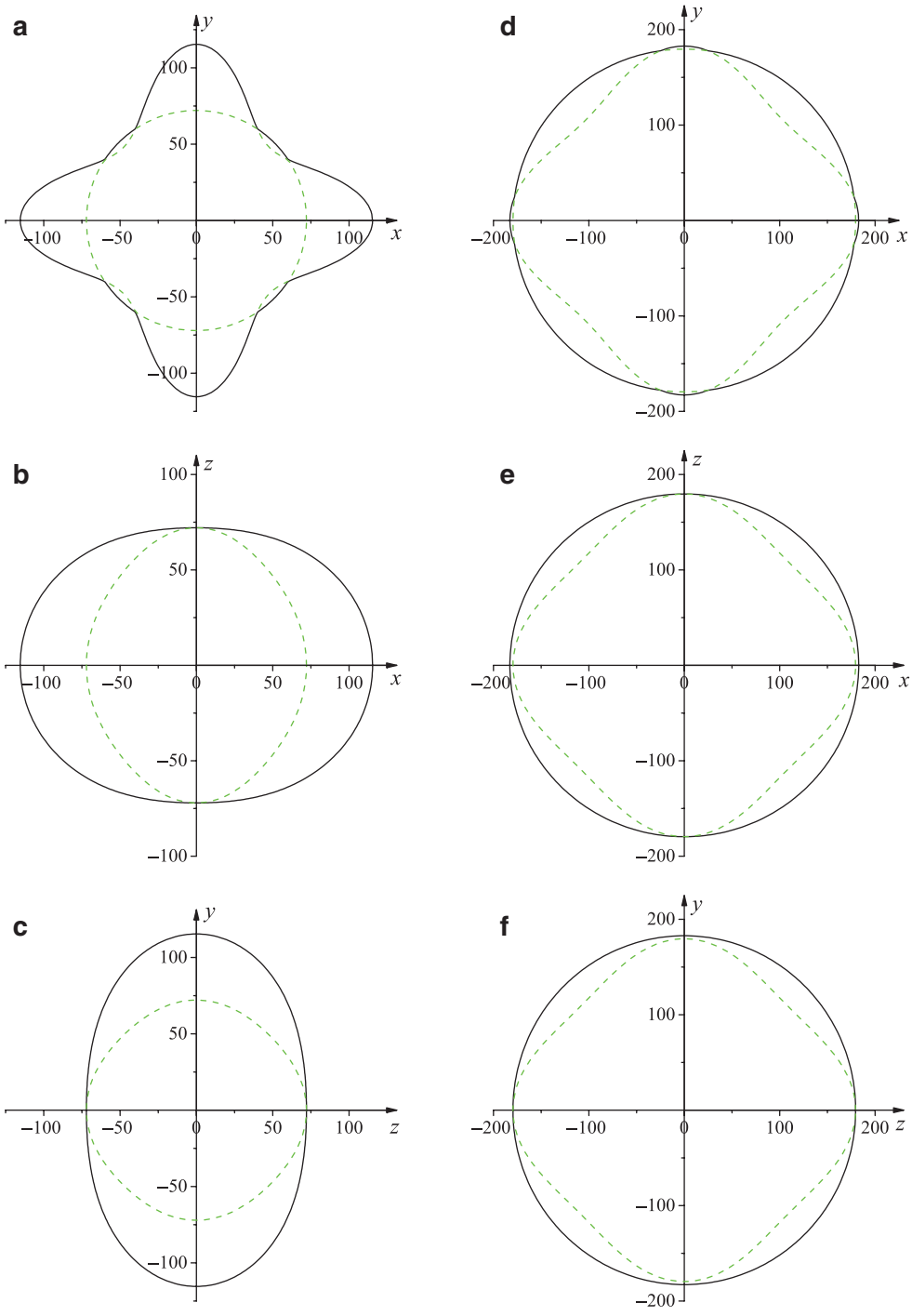

Figure 4: (Color online) Two-dimensional representation of shear modulus in the *xy* plane, *xz* plane, and *yz* plane for $P4_2/mnm$ silicon carbides. The left column (a), (b), and (c) are for Si_8C_4, and the right column (d), (e), and (f) are for Si_4C_8. The black solid line represents the maximum, and the green dashed line represents the positive minimum.

$$\alpha=\frac{(C_{11}-C_{12})(C_{33}-C_{13})-(C_{23}-C_{13})(C_{11}-C_{13})}{(C_{33}-C_{13})(C_{22}-C_{12})-(C_{13}-C_{23})(C_{12}-C_{23})}, \quad (17)$$

$$\beta=\frac{(C_{22}-C_{12})(C_{11}-C_{13})-(C_{11}-C_{12})(C_{23}-C_{12})}{(C_{22}-C_{12})(C_{33}-C_{13})-(C_{12}-C_{23})(C_{13}-C_{23})}. \quad (18)$$

For tetragonal crystal system, the A_{B_a} is always 1.0, whereas the values of A_{B_c} calculated by the method above are 1.825, 1.825, 1.325, and 1.203 for Si_{12}, Si_8C_4, Si_4C_8, and C_{12}, respectively. They are all larger than 1.0, representing the elastic anisotropy.

In addition, we calculated the directional dependence of elastic anisotropy by using the ELAM code [37, 38]. For an isotropic material, the 2D figure should appear perfectly round, while the deviation of the actual shape exhibits the anisotropy. The 2D representation of Young's modulus in

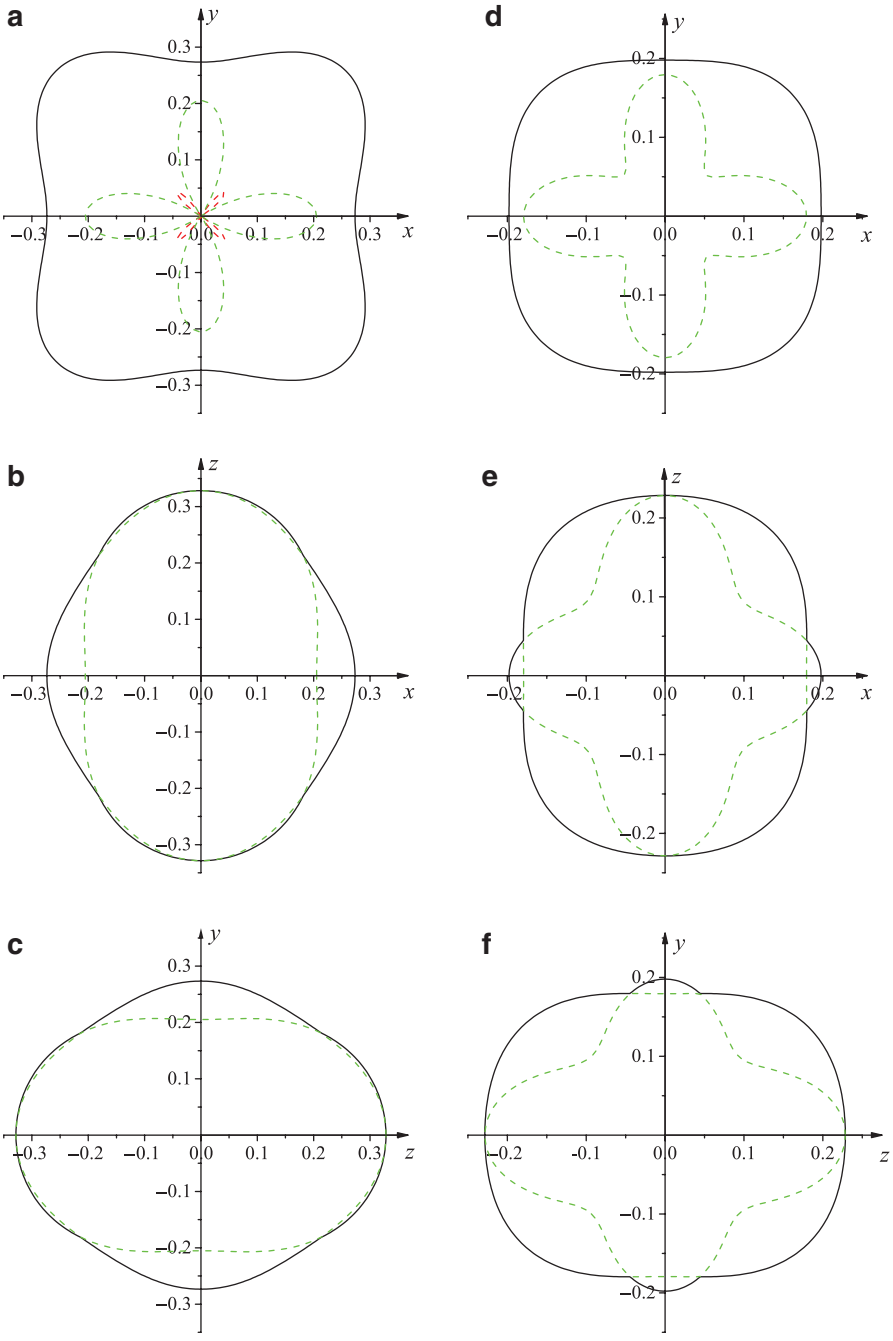

Figure 5: (Color online) Two-dimensional representation of Poisson's ratio in the *xy* plane, *xz* plane, and *yz* plane for $P4_2/mnm$ silicon carbides. The left column (a), (b), and (c) are for Si_8C_4, and the right column (d), (e), and (f) are for Si_4C_8. The black solid line represents the maximum, the red dashed line represents the negative minimum, and the green dashed line represents the positive minimum.

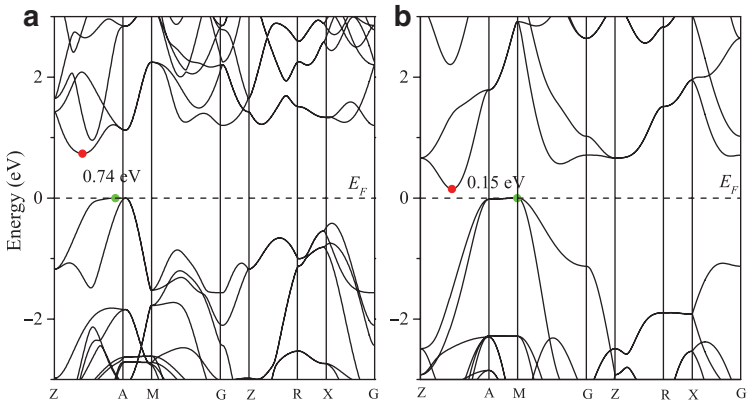

Figure 6: (Color online) Electronic band structure of Si_8C_4 (a) and Si_4C_8 (b). The red dot and green dot represent the CBM and VBM, respectively.

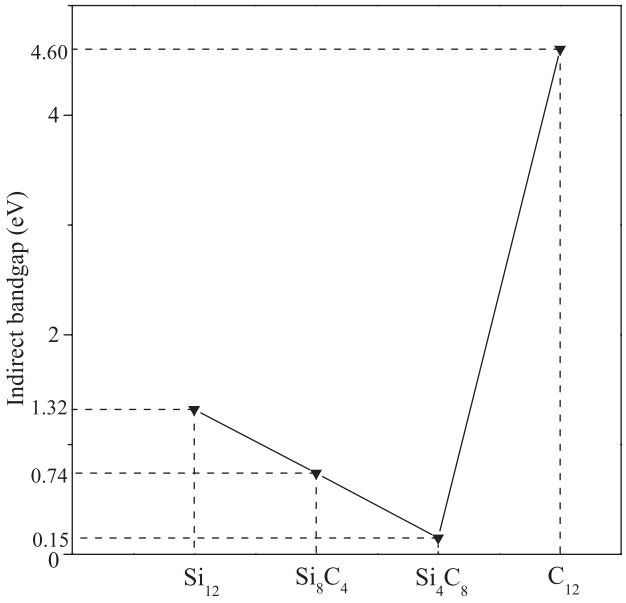

Figure 7: Band gaps of $P4_2/mnm$ silicon carbides versus carbon contents.

different planes are revealed in Figure 3, the left column (a), (b), and (c) are for Si_8C_4, and the right column (d), (e), and (f) are for Si_4C_8. From this figure, we found that, for Si_8C_4, the minimal value of Young's modulus is 160 GPa and the maximal value is 196 GPa, the ratio $E_{max}/E_{min} = 1.23$. For Si_4C_8, the minimal value is 343 GPa and the maximal value is 402 GPa, the ratio $E_{max}/E_{min} = 1.17$. So, both of them exhibit an elastic anisotropy, and the changes of Si_8C_4 along the different directions are more severe. We can see that the maximal value of Young's modulus is on the z-axis, which also conforms the result that C_{33} is the largest in the calculated elastic constants.

Figure 4 shows the 2D representation of shear modulus G, the left column (a), (b), and (c) are for Si_8C_4, and the right column (d), (e), and (f) are for Si_4C_8. The black solid line represents the maximum, and green dashed line represents the positive minimum. For Si_8C_4, $G_{min} = 72$ GPa and $G_{max} = 115$ GPa, the average of G along all directions is 75 GPa, which is close to the 78 GPa shown in Table 3. For Si_4C_8, $G_{min} = 149$ GPa and $G_{max} = 183$ GPa, the average of G along all directions is 170 GPa, which is very close to the calculated value (169 GPa) from (10). And, the ratio of maximum to minimum is 1.6 and 1.23, respectively, indicating an elastic anisotropy. The 2D representation of Poisson's ratio ν in different planes is shown in Figure 5, the left column (a), (b), and (c) are for Si_8C_4, and the right column (d), (e), and (f) are for Si_4C_8. The black solid line represents the maximum, the red dashed line represents the negative minimum, and the green dashed line represents the positive minimum. For Si_8C_4, $-0.06 \le \nu \le 0.33$, we can found that in some particular directions, there will be negative Poisson's ratio. For Si_4C_8, $0.075 \le \nu \le 0.23$. Compared with the aluminum 0.347, they both show a relatively high stiffness. And, they also exhibit the elastic anisotropy.

3.3 Electronic Properties

Calculated electronic band structures of $P4_2/mnm$ silicon carbides at 0 GPa are plotted in Figure 6. The black dashed line represents the Fermi level (E_F). The red dot and green dot represent the conduction band minimum (CBM) and the valence band maximum (VBM), respectively. The band structure of Si_8C_4 is shown in Figure 6(a), the CBM locates at (0.214, 0.214, 0.500) along the Z–A direction, and the VBM locates at (0.476, 0.476, 0.500) along the Z–A direction, and the band gap is 0.74 eV. The band structure of Si_4C_8 is shown in Figure 6(b), the CBM is at (0.231, 0.231,

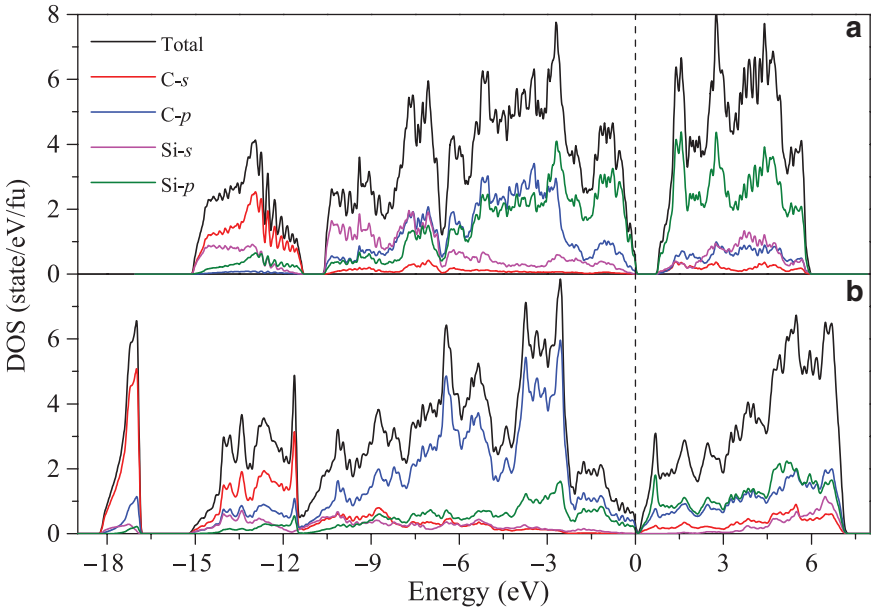

Figure 8: (Color online) The DOS of Si_8C_4 (a) and Si_4C_8 (b).

0.500) along the Z–A direction, and the VBM locates at M point, and the band gap is 0.15 eV. By observing the CBM and the VBM, we conclude that the Si_8C_4 and Si_4C_8 are both the indirect semiconductors. It is known that the band gap calculated by DFT usually should be 30–50 % smaller than the actual values, so the actual band gap will be larger. We also calculated the band gap of C_{12} and Si_{12}, and their band gaps are 4.60 and 1.32 eV, respectively, close to the values 4.55 and 1.28 eV reported in previous works [20]. The changes of band gap are shown in Figure 7, and we found that with the decrease of Si atoms, the band gap is diminishing, except for the C_{12}, whose band gap is much larger than other structures. As we know that for the efficient optoelectronic devices, the value of band gap is crucial. Thereby, we could artificially control the silicon content to choose the needed value.

The density of states (DOSs) of Si_8C_4 is shown in Figure 8(a), and its main features are summarized as follows: (a) the valence band region can be divided into four parts, the first part (–15 to –11 eV) is characterised by the contributions of C-*s* states, the second part (–11 to –8 eV) is mainly due to the Si-*s* states, and the third part (–8 to –6 eV) is originated from the contributions of C-*p* and Si-*s* states. The fourth part (–6 to 0 eV) is mainly due to the mixture of C-*p* and Si-*p* states; moreover, in this part, the partial DOS for both C-*p* and Si-*p* are very similar, reflecting the significant hybridisation between these two orbitals, and showing a strong covalent interaction between the C and Si atoms; (b) The conduction band region is mainly characterised by the Si-*p* states; (c) The DOS near Fermi level is mainly originated from the Si-*p* orbital electrons. Meanwhile, the Si_4C_8 is shown in Figure 8(b), and its main features are similar to the Si_8C_4: (a) the valence band region can be divided into two parts, the first part (–18 to –11 eV) is due to the contributions of C-*s* states, and the second part (–11 to 0 eV) is mainly characterised by the C-*p* states. The conduction band region is mainly due to the mixture contribution of C-*p* and Si-*p* states with the covalent bonding; (b) The C-*p* and N-*p* orbitals in the range of –11 to 7 eV have the significant hybridisation and a strong covalent interaction; (c) The DOS near Fermi level is mainly originated from the mixture contributions of C-*p* and Si-*p* orbital electrons.

4 Conclusions

In summary, we have performed two new $P4_2/mnm$ phase of Si_8C_4 and Si_4C_8, and systematically investigated the structural, elastic, and electronic properties using the first principles calculations. The calculated elastic constants and phonon spectra reveal that the Si_8C_4 and Si_4C_8 are mechanically and dynamically stable. And, the calculations on the bulk modulus, shear modulus, Young's modulus, and Poisson's ratio all exhibit an elastic anisotropy. By calculating the electronic band structures, we conclude that Si_8C_4 and Si_4C_8 are both indirect semiconductors, and their band gaps are 0.74 and 0.15 eV, respectively. In the $P4_2/mnm$ structures, with the decrease of Si atoms, the band gap is diminishing, except for the C_{12}, so we can

choose the needed band gap by controlling the silicon content artificially. Furthermore, we analyse the specific contributions to different parts of the DOS. We believe that more and more theoretical and experimental works will be carried out soon on the novel silicon carbides.

Acknowledgments: This work was financially supported by the Fundamental Research Funds for the Central Universities, Natural Science Foundation of China (No. 61474089), the Fundamental Research Funds for the Central Universities, and Natural Science Basic Research plan in Shaanxi Province of China (Grant No. 2013JQ1007).

References

[1] S. Nakashima and H. Harima, Phys. Stat. Sol. **162**, 39 (1997).
[2] A. R. Verma and P. Krishna, Polymorphism and Polytypism in Crystals, Wiley, New York 1966.
[3] J. C. Han, P. Hu, X. H. Zhang, S. H. Meng, and W. B. Han, Compos. Sci. Technol. **68**, 799 (2008).
[4] J. Zimmermann, G. Hilmas, and W. Fahrenholtz, Mater. Chem. Phys. **112**, 140 (2008).
[5] M. Gasch, D. Ellerby, E. Irby, S. Beckman, M. Gusman, et al., J. Mater. Sci. **39**, 5925 (2004).
[6] S. Zhu, W. Fahrenholtz, and G. Hilmas, J. Eur. Ceram. Soc. **27**, 2077 (2007).
[7] S. X. Dou, S. Soltanian, J. Horvat, X. L. Wang, S. H. Zhou, et al., Appl. Phys. Lett. **81**, 3419 (2002).
[8] S. Guo, J. Yang, H. Tanaka, and Y. Kagawa, Compos. Sci. Technol. **68**, 3033 (2008).
[9] F. Lomello, G. Bonnefont, Y. Leconte, N. Herlin-Boime, and G. Fantozzi, J. Eur. Ceram. Soc. **32**, 633 (2012).
[10] R. Z. Wang, W. G. Li, D. Y. Li, and D. N. Fang, J. Eur. Ceram. Soc. **35**, 2957 (2015).
[11] Q. Y. Fan, C. C. Chai, Q. Wei, H. Y. Yan, Y. B. Zhao, et al., J. Appl. Phys. **118**, 185704 (2015).
[12] Q. Wei, M. G. Zhang, H. Y. Yan, Z. Z. Lin, X. M. Zhu, et al., EPL **107**, 27007 (2014).
[13] Z. Z. Lin, Q. Wei, and X. M. Zhu, Carbon **66**, 504 (2014).
[14] A. K. Geim, Science **324**, 1530 (2009).
[15] C. Berger, Science **312**, 1191 (2006).
[16] C. Riedl, C. Coletti, T. Iwasaki, A. A. Zakharov, and U. Starke, Phys. Rev. Lett. **103**, 246804 (2009).
[17] K. V. Emtsev, F. Speck, T. Seyller, L. Ley, and J. D. Riley, Phys. Rev. B **77**, 155303 (2008).
[18] F. Varchon, R. Feng, J. Hass, X. Li, B. N. Nguyen, et al., Phys. Rev. Lett. **99**, 126805 (2007).
[19] T. Ohta, Science **313**, 951 (2006).
[20] M. C. Nguyen, X. Zhao, C.-Z. Wang, and K. -M. Ho, Phys. Rev. B **89**, 184112 (2014).
[21] P. Hohenberg and W. Kohn, Phys. Rev. **136**, B864 (1964).
[22] W. Kohn and L. J. Sham, Phys. Rev. **140**, A1133 (1965).
[23] D. M. Ceperley and B. J. Alder, Phys. Rev. Lett. **45**, 566 (1980).
[24] J. P. Perdew and A. Zunger, Phys. Rev. B **23**, 5048 (1981).
[25] J. P. Perdew, K. Burke, and M. Ernzerhof, Phys. Rev. Lett. **77**, 3865 (1996).
[26] S. J. Clark, M. D. Segall, C. J. Pickard, P. J. Hasnip, M. I. J. Probert, et al., Z. Kristallogr. **220**, 567 (2005).
[27] B. G. Pfrommer, M. Cote, S. G. Louie, and M. L. Cohen, J. Comput. Phys. **131**, 233 (1997).
[28] H. J. Monkhorst and J. D. Pack, Phys. Rev. B **13**, 5188 (1976).
[29] Z. J. Wu, E. J. Zhao, H. P. Xiang, X. F. Hao, X. J. Liu, et al., Phys. Rev. B **76**, 054115 (2007).
[30] W. Voigt, Lehrburch der Kristallphysik, Teubner, Leipzig 1928.
[31] A. Reuss, Z. Angew. Math. Mech. **9**, 49 (1929).
[32] R. Hill, Proc. Phys. Soc. London **65**, 349 (1952).
[33] D. M. Teter, Mater. Res. Soc. Bull. **23**, 22 (1998).
[34] S. F. Pugh, Philos. Mag. **45**, 823 (1954).
[35] W. X. Feng, S. X. Cui, H. Q. Hu, P. Feng, Z. Y. Zheng, et al., Physica B **405**, 4294 (2010).
[36] P. Ravindran, L. Fast, P. A. Korzhavyi, B. Johansson, J. Wills, et al., J. Appl. Phys. **84**, 4891 (1998).
[37] A. Marmier, Z. A. D. Lethbridge, R. I. Walton, C. W. Smith, S. C. Parker, et al., Comput. Phys. Commun. **181**, 2102 (2010).
[38] Q. Y. Fan, Q. Wei, C. C. Chai, M. G. Zhang, H. Y. Yan, et al., Comput. Mater. Sci. **97**, 6 (2015).